ACS OMEGA

http://pubs.acs.org/journal/acsodf

Article

Effect of Polymer Nano- and Microparticles on Calcium Carbonate Crystallization

Gomathi Mahadevan, Qiu Ruifan, Yap Hui Hian Jane, and Suresh Valiyaveettil*

Cite This: *ACS Omega* 2021, 6, 20522−20529

Read Online

ACCESS | Metrics & More | Article Recommendations | Supporting Information

ABSTRACT: Molecular and macromolecular templates are known to affect the shape, size, and polymorph selectivity on the biomineralization of calcium carbonate ($CaCO_3$). Micro- and nanoparticles of common polymers present in the environment are beginning to show toxicity in living organisms. In this study, the role of plastic nanoparticles in the biomineralization of $CaCO_3$ is explored to understand the ecological impact of plastic pollution. As a model study, luminescent poly(methyl methacrylate) nanoparticles (PMMA-NPs) were prepared using the nanoprecipitation method, fully characterized, and used for the mineralization experiments to understand their influence on nucleation, morphology, and polymorph selectivity of $CaCO_3$ crystals. The PMMA-NPs induced calcite crystal nucleation with spherical morphologies at high concentrations. Microplastic particles collected from a commercial face scrub were also used for $CaCO_3$ nucleation to observe the nucleation of calcite crystals on the particle surface. Microscopic, spectroscopic, and X-ray diffraction data were used to characterize and identify the nucleated crystals. The data presented in this paper add more information on the impact of microplastics on the marine environment.

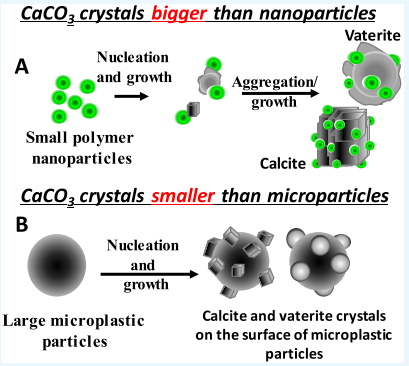

INTRODUCTION

Biomineralization is a process involving biosynthesis of minerals with specific size, morphology, and orientation under ambient environmental conditions.[1−3] This process is often characterized as a fascinating material synthesis in which minerals and organic components interact at different hierarchical levels to control nucleation, growth, and morphology of the deposited minerals. Calcium carbonate ($CaCO_3$) is one of the most abundant minerals present in the environment,[4,5] which plays a significant role in the formation of shells and other hard functional architectures in many marine organisms.[6] The three common crystalline polymorphs of $CaCO_3$ (i.e., calcite, aragonite, and vaterite) are nucleated under different conditions.[7−9] Calcite is present in exoskeletons of vertebrates and invertebrates under normal conditions.[10] The shells of marine mollusks and echinoderms are widely made of the aragonite polymorph.[10,11] Stable vaterite phase was observed in some parts of the malformed Corbicula's shells.[12]

During the past three decades, plastic wastes have been accumulating in the environment due to widespread usage, improper disposal, high stability, and low rate of recycling. The environmental degradation of plastics generates small particles, which are known as microplastics (<5 mm) and nanoplastics (<1 μm).[13] Such particles are present in all types of ecosystems and contaminate the potable water supply and food security of the population.[14] In general, smaller particles enter and translocate inside the cells and tissues much more readily than larger ones. Continuous accumulation of micro- and nanoparticles (NPs) of plastics is known to cause adverse health effects such as physiological stress,[13] feeding alteration,[15] growth retardation,[16] fertility reduction,[17] and decrease in survival rate,[18,19] to name a few problems in marine organisms. Recently, we explored the environmental impact of polymer nanoparticles using barnacle as a model system.[20] Also, the uptake of polymer nanoparticles by human cells exposed to moderate to high concentrations was examined in detail.[21]

Many organic molecules and polymers are reported to control the nucleation,[22] orientation,[23] growth kinetics,[24] and morphology of $CaCO_3$ under in vitro and in vivo conditions.[25−27] Since the environment is contaminated with large amounts of plastic particles and the living organisms are continuously ingesting them, it is interesting to explore the influence of micro- and nanoparticles of common plastics on the mineralization of $CaCO_3$ under in vitro conditions. Such knowledge helps us to understand the impact of plastic pollution on the health of marine vertebrates and invertebrates. In this study, the effects of luminescent nanoparticles prepared from poly(methyl methacrylate) (PMMA-NPs) and micro-

Received: May 16, 2021
Accepted: June 16, 2021
Published: July 28, 2021

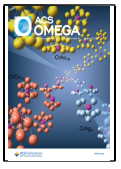

plastic particles extracted from a commercial face scrub on the nucleation, growth, and polymorph selectivity of $CaCO_3$ crystals are explored. In addition, the effects of experimental parameters such as concentration of PMMA-NPs and crystallization time are also examined. The fluorescence properties help to track the PMMA-NPs on the $CaCO_3$ crystals using a fluorescence microscope.

RESULTS AND DISCUSSION

Characterization of Polymer Nanoparticles. The fluorescent PMMA-NPs were prepared using a published procedure.[20,28] The obtained particles were characterized using spectroscopy techniques like optical microscopy, scanning electron microscopy (SEM), and dynamic light scattering (DLS) (Figures 1 and S1). UV−vis spectrum (Figure 1a) of

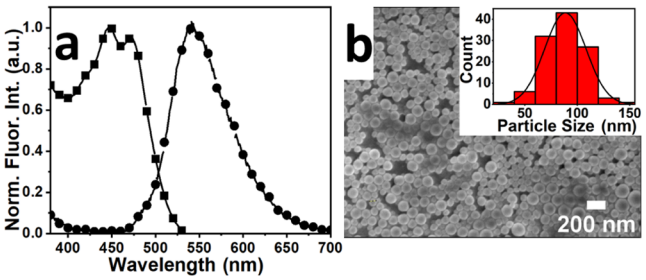

Figure 1. (a) Absorption (■) and emission (●) spectra of PMMA-NPs in water. (b) SEM image of relatively monodispersed nanoparticles with spherical morphologies; the inset shows particle size distribution. The calculated average size of the PMMA-NPs was 88 nm.

the polymer nanoparticles revealed two absorbance peaks at 445 and 470 nm, characteristic of the perylenetetraester (PTE) dye encapsulated inside the particle. The fluorescence spectrum (Figure 1a) of PMMA showed a broad maximum at 540 nm. Both absorbance and fluorescence spectra are consistent with the spectrum of encapsulated dye perylenetetraester.[20] The inset in Figure 1b shows the size distribution profile of spherical PMMA-NPs with an average size of 88 nm. The hydrated particle size obtained from DLS measurement was 130 nm for PMMA-NPs. The hydrated radius from DLS measurement is usually larger than the dry radius obtained from SEM data. The surface charge measured for the PMMA-NPs dispersed in water was ca. -24.5 ± 0.3 mV.

Effect of the Concentration of PMMA-NPs on $CaCO_3$ Crystallization. To understand the effect of PMMA-NPs on the nucleation and growth of $CaCO_3$ crystals, the crystallization experiments were carried out using a range of concentrations (25, 50, 75, and 125 μg/mL) of particles. At a lower concentration (i.e., 25 μg/mL), PMMA-NPs induced the nucleation of calcite crystals (Figure 2a), similar to control samples with no polymer particles added (Figure S2). At higher concentrations (i.e., 50, 75 μg/mL), the morphologies of crystals nucleated have changed from rhombohedral to irregular or spherical shape (Figure 2b,c). Only spherical crystals were nucleated at a high concentration (125 μg/mL) of the PMMA-NPs (Figure 2d). The white spots seen on the crystals are aggregates of polymer particles deposited on the surface of crystals. The optical and SEM images of $CaCO_3$ crystals nucleated in the absence of PMMA-NPs showed the expected rhombohedral calcite crystals (Figures S2 and 3d−f). As a control and to confirm that the morphological changes

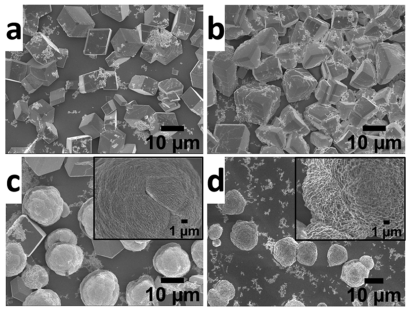

Figure 2. Scanning electron microscopy images of $CaCO_3$ crystals nucleated in the presence of PMMA-NPs at different concentrations of 25 μg/mL (a), 50 μg/mL (b), 75 μg/mL (c), and 125 μg/mL (d) under ambient conditions. The insets in (c) and (d) indicate the enlarged view of the single crystal surface. The SEM image of rhombohedral calcite crystals of $CaCO_3$ obtained in the absence of PMMA-NPs is given in the Supporting Information (Figure S2).

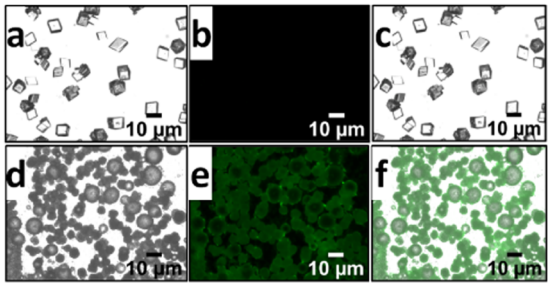

Figure 3. Optical images of $CaCO_3$ crystals nucleated in the presence (a−c) and absence (d−f) of PMMA-NPs under differential interference contrast (DIC) (a, d), fluorescein isothiocyanate (FITC) (b, c), and filters and merged condition (c, f). The concentration of PMMA-NPs used for crystallization was 125 μg/mL. Only fluorescent emissions from the PMMA-NPs and not the actual particles are observed on the surface of the crystals due to the low resolution of the optical microscope.

were not due to the presence of stabilizing agent, sodium dodecyl sulfate (SDS) used to stabilize the nanoparticles, same amounts of SDS were added into the precursor $CaCl_2$ solution and the crystallization was carried out under identical conditions. SEM images of $CaCO_3$ crystals nucleated in the presence of SDS (Figure S3) showed aggregation of the rhombohedral calcite crystals but no significant changes in shapes. Thus, the observed changes in morphology (Figures 2 and 3a−c) were due to the influence of PMMA-NPs. The crystal growth in solution is sensitive to the methods employed. For example, Parakhonskiy et al. reported that the $CaCO_3$ crystals with different shapes (e.g., spherical, cubic, elliptical, starlike) are obtained by controlling the crystallization conditions.[29] Similarly, nanodisks and nanorods of $CaCO_3$ composites were obtained by fine-tuning the composition of the crystallization solution containing poly(acrylic acid) (PAA)-stabilized amorphous calcium carbonate (ACC) precursors.[30]

The presence of fluorescent PMMA-NPs on the surface of nucleated $CaCO_3$ crystals was investigated using a fluorescence microscope (Figure 3). Figure 3a−c shows images of $CaCO_3$ crystals collected in the absence of polymer nanoparticles. Similarly, the crystal growth under the same condition, but in the presence of PMMA-NPs at a 125 μg/mL concentration is shown in Figure 3d−f. The images are obtained using differential interference contrast (DIC, Figure 3a,d), fluo-

https://doi.org/10.1021/acsomega.1c02564
ACS Omega 2021, 6, 20522−20529

rescein isothiocyanate (FITC, Figure 3b,e), and filter and merged images (Figure 3c,f) to highlight the presence of PMMA particles on the crystal surface. The fluorescent micrographs of crystals obtained at lower concentrations (25, 50, 75 μg/mL) of PMMA-NPs are shown in the Supporting Information (Figure S4). The observed green fluorescence from the crystals is due to the presence of dye encapsulated polymer nanoparticles on the surface of the crystals. FITC channel was used to image the green fluorescence from the PTE dye encapsulated inside the polymer nanoparticles.

Since the dye is not soluble in water and does not leach out of the PMMA-NPs, it is important to note that the observed green fluorescence implies the presence of PMMA-NPs on the surface of the crystals. Optical micrographs of calcite crystals grown in the absence of nanoparticles showed the regular rhombohedral calcite crystal morphology with no green fluorescence (Figure 3a−c). Both SEM and optical images indicate that polymer nanoparticles interact strongly with the crystal surfaces and are responsible for the observed changes in morphologies of the crystals.

The Fourier transform infrared (FTIR) spectra (Figure 4a) of $CaCO_3$ crystals grown in the presence of PMMA-NPs at

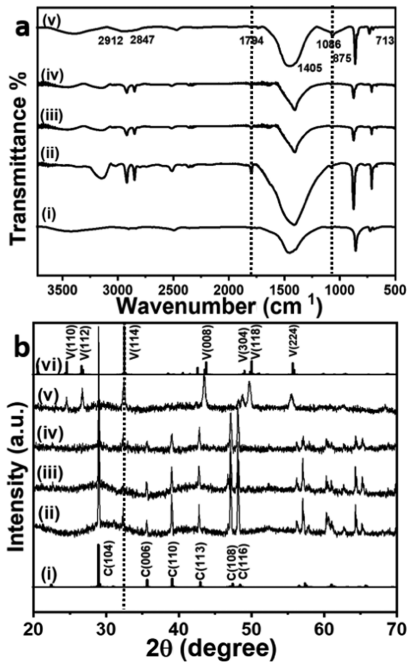

Figure 4. FTIR (a) and X-ray diffraction (XRD) spectra of (b) $CaCO_3$ crystals nucleated in the presence of different concentrations, 0 μg/mL (i), 25 μg/mL (ii), 50 μg/mL (iii), 75 μg /mL (iv), and 125 μg/mL (v) of PMMA-NPs. The standard FTIR (a, i) and XRD pattern of calcite ((i) PDF # 05-0586) and vaterite phase ((vi) PDF #33-0268) are also given for comparison.

different concentrations were recorded using KBr as the matrix.[31,32] Control samples (Figure 4a(i)) collected without adding the PMMA-NPs showed sharp peaks at 874 and 713 cm^{-1}, which correspond to the υ_4 and υ_2 absorption peaks of the calcite phase. The broad peak at 1405−1450 cm^{-1} (υ_3) is attributed to the absorption peaks of the carbonate group. At low concentrations of PMMA-NPs (25 and 50 μg/mL), two peaks at 874 and 713 cm^{-1} corresponding to the calcite phase were observed (Figure 4a(ii−iv)).[33] The broad absorbance observed at 1405 cm^{-1} is assigned to the symmetric stretching vibration of carbonate ($-CO_3^{2-}$) group.[33] A characteristic small peak around 1794 cm^{-1} (Figure 4a(ii−v)) was attributed to >C═O of the ester groups of PMMA interacting strongly with calcium ions.[34−36] The peak appearing at 1086 cm^{-1} is assigned to the vaterite phase (Figure 4a(v)).[37] Also, the peaks observed in the 2912−2921 and 2842−2847 cm^{-1} regions correspond to the C−H stretching vibration of the PMMA-NPs present in the sample.[38] This is consistent with the fluorescence images given in Figure 3.

Figure 4b shows the XRD patterns of $CaCO_3$ crystals grown in the presence of different concentrations of PMMA-NPs. All diffraction patterns are assigned via comparison with the published standard powder diffraction (PDF) pattern of $CaCO_3$ polymorphs (calcite—PDF #05-0586 and vaterite PDF #33-0268). XRD patterns of pure calcite and vaterite crystals are given in Figure 4b(i,vi), respectively. The crystals nucleated in the presence of PMMA-NPs showed diffraction peaks appearing at 2θ values of 29.0° (104), 32.4° (006), 35.5° (110), 39.0° (113), 47.1° (108), and 48.1° (116) corresponding to the calcite phase (Figure 4b(ii−iv)). At a high concentration of 125 μg/mL (Figure 4b(v)), vaterite peaks were observed at 24.4° (110), 26.6° (112), 32.2° (114), 43.4° (008), 48.8° (304), 49.7° (118), and 55.4° (224). SEM images (Figure 2a,b) also support that at lower concentrations (25, 50 μg/mL), majority of crystals nucleated were of the calcite phase with rhombohedral shape, whereas at higher concentrations (Figure 2c,d), a spherical vaterite phase was observed.

From the XRD data (Figure 4b), the percentage of each $CaCO_3$ phase was calculated using eq 2.[34]

$$\frac{I_c^{104}}{I_v^{110}} = \Delta \times \frac{X_c}{X_v} \quad (1)$$

$$X_v = \frac{7.691\, I_v^{110}}{I_c^{104} + 7.691\, I_v^{110}};\ X_c = 1 - X_v \quad (2)$$

where I_c^{104} and I_v^{110} are the intensities of (104) and (110) planes, respectively, and X_c and X_v are the molar content (%) of the calcite and vaterite phases, respectively.

The calculated percentage of the polymorphs from various concentrations of PMMA-NPs is shown in Figure 5. The data suggests that the addition of PMMA-NPs on $CaCO_3$ crystallization has no observable effect up to a concentration of 75 μg/mL. However, at high concentrations (>75 μg/mL),

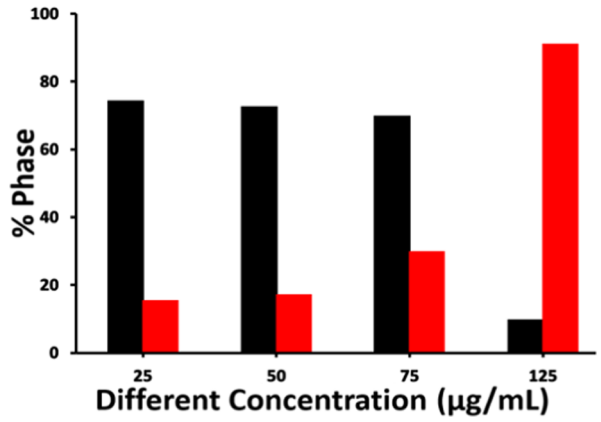

Figure 5. Percentage distribution of polymorph calcite (black solid bar) and vaterite (red solid bar) on the addition of PMMA-NPs at different concentrations.

https://doi.org/10.1021/acsomega.1c02564
ACS Omega 2021, 6, 20522−20529

vaterite phase (91.2%) was formed predominantly and a very small amount (8.8%) of calcite phase was nucleated (Figure 5). Similar results were reported earlier in the presence of SDS-modified poly(vinylpyrrolidone) (PVP) nucleated flower and spherical-shaped $CaCO_3$ crystals at different polymer concentrations.[39−41] Control experiments were done using different concentrations of SDS, and only calcite crystals with aggregated rhombohedral shapes were nucleated (Figure S3).

Characterization of the Microplastic Particles from Facial Scrub. A preliminary experiment was done to establish the nature of the microplastic particles present in a commercial face scrub and its impact on $CaCO_3$ crystal nucleation and growth. A facial scrub from a local shop was purchased, and microplastic particles were collected through filtration and washing. Two types of particles were extracted from the facial scrub, white and green. These particles were dispersed in deionized (DI) water (20 mg in 1 mL), and small aliquots (100 μL) from this stock solution were used for characterization and crystallization experiments.

The FTIR spectra of green and white particles separated from facial scrub are given in the Supporting Information (Figure S5). The major peaks for the hydroxyl groups were observed at 3100−3400 cm^{-1}, C−H stretching showed a broad peak in the 2800−3000 cm^{-1} region, and a strong peak was observed at 1086, indicating the C−O stretching vibration of the primary alcohol.[42] Peaks at 799 and 952 are attributed to C−H bending. Thus, the white solid was identified as microcrystalline cellulose particles.[42] The green particles showed characteristic strong peaks at 2920 and 2850 cm^{-1} attributed to the C−H stretching vibration and peaks at 1468 and 722 cm^{-1} due to C−H bending vibrations of polyethylene (PE).[43,44]

The SEM micrograph of pure calcite crystals grown in the absence of any polymer particles is given in Figure 6a. Both white and green particles after multiple washings with water showed a size range of 200−300 μm (Figure 6b). The microplastic extracted from the facial scrub showed spherical morphology (Figure 6b). Upon crystallization of $CaCO_3$, both green (PE) and white (cellulose) microplastic particles nucleated calcite crystals on the surface (Figure 6c,d). The effect of other chemicals present in the scrub was also examined by adding a small amount in the crystallization medium. In the absence of microplastic particles, a small amount (10 μL) of the scrub solution nucleated mostly truncated rhombohedral calcite crystals with a few stacked or aggregated morphology (Figure S6). However, in the presence of microplastic particles, a large number of small spherical or truncated particles of calcite crystals were nucleated on the surface of both microplastic particles (Figure 6e,f). This clearly demonstrates that the microplastic particles are active toward the nucleation and growth of $CaCO_3$ crystals on their surface.

FTIR spectra of crystals grown on the microplastic particles after crystallization were recorded and are given in Figure 7a.

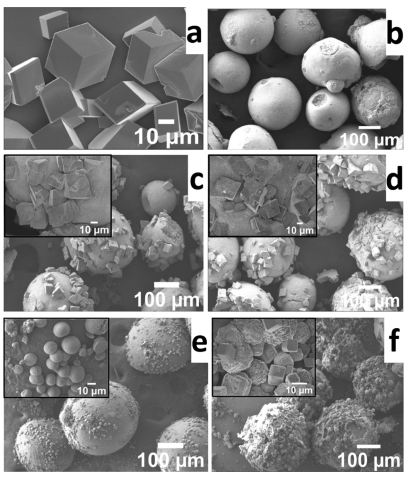

Figure 6. SEM images of pure $CaCO_3$ crystals (a), microplastic particles extracted from the facial scrub (b), $CaCO_3$ crystals grown on clean washed green (c), white (d) microplastic particles, green particles + soap solution (e), and white particles + soap solution (f). The insets in (c)−(f) show an expanded region of the surface of the particles. The stock solution of particles (100 μL) and soap solution (10 μL) were used for crystallization.

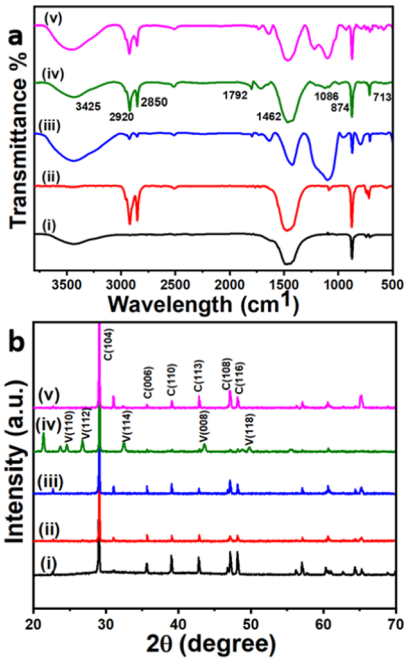

Figure 7. FTIR (a) and XRD spectra (b) of calcite crystals in the absence of any additives (i), in the presence of green (ii) and white (iii) microplastic particles, green particles + soap solution (iv), and white particles + soap (v) extracted from scrub are given for comparison.

As discussed above, the peaks observed at 713 and 874 cm^{-1} in the FTIR spectra of $CaCO_3$ showed the presence of calcite phase (Figure 7a(i)). Such peaks are also observed when calcite crystals formed under the influence of green particles (Figure 7a(ii)) and the white particles (Figure 7a(iii)). In addition to the calcite peaks, both green and white particles under the influence of soap (Figure 7a(iv)) showed a peak for the vaterite phase at 1086 cm^{-1}. All characteristic peaks described above for functional groups such as −OH (3100−3400 cm^{-1} for cellulose), C−H (2850 and 2920 cm^{-1} for both cellulose and PE), C−O (1086 and 1462 cm^{-1} for cellulose), and peaks at 713 and 874 cm^{-1} for the calcite phase were also observed (Figure 7a(i−iv)).

The XRD spectrum of crystals grown in the absence of particles showed strong characteristic calcite peaks at 2θ = 29.9° (104) along with other expected peaks described above (Figure 7b(i)). Both white and green particles extracted from the face scrub showed the nucleation of calcite crystals with the

https://doi.org/10.1021/acsomega.1c02564
ACS Omega 2021, 6, 20522−20529

peaks corresponding to 2θ values of 29.0° (104), 32.4° (006), 35.5° (110), 39.0° (113), 47.1° (108), and 48.1° (116) (Figure 7b(ii,iii)). Under the influence of soap solution, green PE microplastic particles nucleated both calcite and vaterite crystals on the surface (Figure 7b(iv)), while the white cellulose particles induced the nucleation of only calcite crystals. The low intensity of the vaterite crystals in the FTIR spectrum (Figure 7a(iv)) implies that the relatively low-concentration vaterite crystals on the surface of the microplastic particles. In addition to the peaks that belong to the calcite phase, the peaks appearing at 2θ values of 24.4° (110), 26.6° (112), 32.2° (114), 43.4° (008), and 49.7° (118) correspond to the vaterite phase (Figure 7b(iv)). White particles along with soap solution (Figure 7b(v)) induced the nucleation of calcite crystals, which was confirmed by the appearance of 2θ peaks at 29.0° (104), 32.4° (006), 35.5° (110), 39.0° (113), 47.1° (108), and 48.1° (116).

Mechanism of Nucleation. A schematic representation of the observed crystal growth in the presence of polymer nanoparticles and microplastic particles is given in Figure 8.

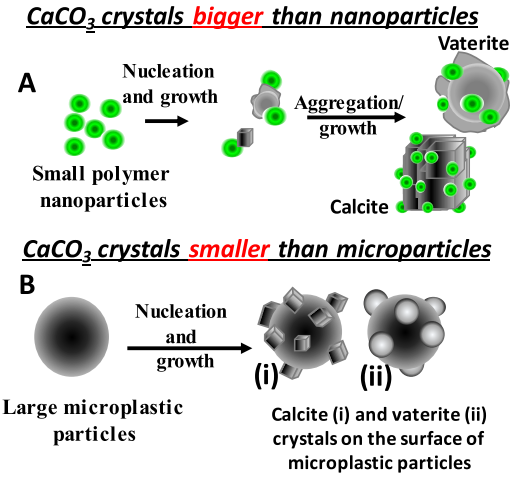

Figure 8. Schematic representation of the predominant $CaCO_3$ nucleation on polymer particles under different conditions.

The general crystal growth mechanism comprises two stages, nucleation and growth. The chemical nature and organization of functional groups on the surface of polymer nanoparticles are important toward recognition of the calcium or carbonate ions from solution, followed by saturation on the surface of the particles, which then leads to nucleation, growth, and control on the overall morphology of the crystal. In this study, we used two types of particles—luminescent polymer nanoparticles, which are smaller than the calcite crystals nucleated (Figure 8A), and nonluminescent PE and cellulose microparticles, which are much bigger than the calcite or vaterite crystals nucleated (Figure 8B). If the concentration of Ca^{2+} ions is kept constant, an increase in polymer particle concentration reduces the growth and size of the calcite crystals formed due to the large number of nucleating sites. We are working on developing the mechanism of nucleation of both calcite and vaterite crystals in the presence of a high concentration of the polymer nanoparticles.

The negative surface charges and functional groups on the surface of polymer particles help us to attract the positively charged Ca^{2+} ions, which then act as nucleating sites. Since polymer nanoparticles are relatively small, the growing calcite crystals tend to aggregate in the presence of PMMA-NPs (Figure 2c,d). The opposite scenario is seen in the case of large microplastic particles, where multiple individual rhombohedral calcite crystals are observed on the surface of large polymer particles. If there are no organic compounds or active molecules present in the solution to control the polymorph or the morphology, a regular rhombohedral shape for all calcite crystals was observed. In the presence of soap solution, the morphology seems to change from rhombohedral to spherical shape for the calcite crystals. In addition, the ester groups of PMMA on the particle surface are expected to interact with Ca^{2+} ions in solution.[45−48] Both polymer particle surfaces offer a large number of nucleation sites, which then speed up the crystal nucleation and growth processes. Currently, we are exploring the formation of the vaterite crystals at high concentrations of the polymer nanoparticles.

CONCLUSIONS

Here, luminescent PMMA-NPs with a hydrodynamic size of 130 nm were prepared and used for crystallization of $CaCO_3$ to understand the role of polymer particles and surface functional groups in the nucleation and growth of the crystals and polymorph selectivity. The negatively charged PMMA-NPs influenced the nucleation of calcite crystals from solution. Rhombohedral calcite crystals were nucleated at lower concentrations (25−50 μg/mL), and a mixture of calcite and spherical vaterite crystals was obtained at a higher concentration (125 μg/mL) of PMMA-NPs. Fluorescence microscopy and FTIR data showed the presence of PMMA-NPs on the surface of nucleated crystals. In addition, a few polymer microparticles (i.e., PE and cellulose) were collected from a commercial face scrub, cleaned, characterized, and used for crystallization experiments. Such large particles also showed the nucleation of calcite or vaterite crystals on the surface. The influence of the other chemicals present in the scrub is not very clear due to the lack of information on the nature of additives present in the face scrub solution. Overall, both synthesized PMMA-NPs and the polymer microparticles obtained from commercial face scrub induced the nucleation of calcite and vaterite crystals based on the concentrations of the particles used. Such observations are important due to the increasing concentrations of polymer nano- and microparticles in the environment.

MATERIALS AND METHODS

Materials. Reagent-grade poly(methyl methacrylate) (PMMA, M_w 350 000), sodium dodecyl sulfate (SDS), acetone, tetrahydrofuran (THF), calcium chloride dihydrate ($CaCl_2{\cdot}2H_2O$), and ammonium carbonate ($(NH_4)_2CO_3$) were purchased from Sigma-Aldrich and used without further purification. Perylenetetraester dye (PTE) was synthesized using a previously described procedure.[49] Deionized water was used throughout the experiment.

Characterization Technique. UV−vis spectra of poly(methyl methacrylate) nanoparticles (PMMA-NPs) were recorded using a UV-1800 Shimadzu spectrophotometer. The fluorescence spectra were recorded on an Agilent Cary Eclipse Fluorescence spectrophotometer. The images were captured under differential interference contrast (DIC) and fluorescein isothiocyanate (FITC) filters. Hydrodynamic radii and ζ-potential of the particles in water were measured using a Malvern Zeta Sizer instrument. The morphology of $CaCO_3$

https://doi.org/10.1021/acsomega.1c02564
ACS Omega 2021, 6, 20522−20529

crystals collected on the coverslips was established using an Olympus EVOS7000 optical fluorescence microscope and a JEOL JSM-6701F scanning electron microscope (SEM). The composition of $CaCO_3$ was analyzed using a Shimadzu model Fourier transform infrared (FTIR) Prestige-21 spectrophotometer within the range of 4000−400 cm^{-1}. The crystal lattice structure of the $CaCO_3$ samples was investigated using a Bruker D8 Advance Powder Crystal X-ray diffractometer with Cu Kα radiation (λ = 0.154 nm) within a 2θ range of 10−70° and source at 40 kV and 40 mA.

Nanoprecipitation. PMMA-NPs were prepared using a nanoprecipitation method as reported in the literature.[20,28] Briefly, the PMMA (250 mg, M_w = 350 000), SDS (10 mg, 4 wt % of the polymer), and PTE (12.5 mg, 5 wt % of the polymer) were dissolved in acetone or tetrahydrofuran (100 mL). An aliquot of the polymer solution (5 mL) was transferred into water (50 mL) and kept for stirring overnight under ambient conditions to evaporate the organic solvent. The aqueous clear solution was then dialyzed to remove all free molecules in solution and filtered using cotton plugs to remove large particles and debris. The PMMA-NPs in the resulting filtrate were characterized using dynamic light scattering (DLS), UV−vis spectroscopy (UV−vis), optical microscope, fluorescence spectroscopy, and scanning electron microscopy (SEM).

$CaCO_3$ Crystallization. Crystallization of $CaCO_3$ was performed using a slow gas diffusion method according to a reported procedure.[50] Briefly, $CaCl_2{\cdot}2H_2O$ solution (3 mL, 0.05 M) was mixed with appropriate amounts of PMMA-NP solution of varying concentration[s] (25, 50, 75, and 125 μg/mL). Pre-cleaned glass coverslips were placed inside the solution, and the whole setup was kept inside a desiccator containing excess $(NH_4)_2CO_3$ solid. After 48 h, the coverslips were removed, washed with water, and dried at room temperature. Control experiments were performed simultaneously using same concentrations of $CaCl_2$, but in the absence of polymer particle solutions. All crystals collected were characterized using a range of techniques such as optical microscopy, scanning electron microscopy, X-ray diffraction, and FTIR spectroscopy.

Crystallization in the Presence of Microplastic from Commercial Face Scrub. To check the effect of microplastic particles present in a commercial face scrub, an appropriate amount (10 mL) was diluted with water, filtered to collect the microplastic particles, washed with DI water (5 × 100 mL), and the collected particles (20 mg) were redispersed in DI water (1 mL). An aliquot of this solution (100 μL) was added to $CaCl_2$ solution (3 mL, 0.05 M) and kept for crystallization. Coverslips were introduced into the solution before being kept inside a desiccator containing $(NH_4)_2CO_3$ solid. After 48 h, the coverslips were taken out, washed with water, and dried at room temperature. The dried samples were fully characterized using a range of techniques such as optical microscopy, scanning electron microscopy, X-ray diffraction, and FTIR spectroscopy. As controls, different crystallization experiments were carried out with (i) no additives and (ii) the soap solution (10 μL). The crystallization was performed using a $CaCl_2$ solution (3 mL, 0.05 M) through a gas diffusion method as described above. The coverslips were removed after 48 h, washed with water, and used for further characterization.

■ ASSOCIATED CONTENT

Supporting Information

The Supporting Information is available free of charge at https://pubs.acs.org/doi/10.1021/acsomega.1c02564.

DLS data of PMMA-NPs prepared from nanoprecipitation, SEM micrographs of $CaCO_3$ crystals nucleated in the absence of PMMA-NPs or other additives, SEM images of $CaCO_3$ crystals obtained in the presence of pure SDS at different concentrations, optical fluorescence images of $CaCO_3$ crystals nucleated under different concentrations (1−10 μg/mL) of PMMA-NPs, FTIR and XRD spectra of green and white microparticles extracted from the commercial face scrub, and SEM image of $CaCO_3$ crystals nucleated under the influence of aqueous scrub solution (PDF)

■ AUTHOR INFORMATION

Corresponding Author

Suresh Valiyaveettil − *Department of Chemistry, National University of Singapore, 117543, Singapore*; orcid.org/0000-0001-6990-660X; Email: chmsv@nus.edu.sg

Authors

Gomathi Mahadevan − *Department of Chemistry, National University of Singapore, 117543, Singapore*

Qiu Ruifan − *Department of Chemistry, National University of Singapore, 117543, Singapore*

Yap Hui Hian Jane − *Department of Chemistry, National University of Singapore, 117543, Singapore*

Complete contact information is available at: https://pubs.acs.org/10.1021/acsomega.1c02564

Funding

Singapore Ministry of Education Tier-1 grant, R-143-000-A76-114.

Notes

The authors declare no competing financial interest.

■ ACKNOWLEDGMENTS

The authors acknowledge the funding support from Ministry of Education Tier-1 grant, R-143-000-A76-114 and technical support from the Department of Chemistry at the National University of Singapore.

■ REFERENCES

(1) Gower, L. B. Biomimetic Model Systems for Investigating the Amorphous Precursor Pathway and Its Role in Biomineralization. *Chem. Rev.* **2008**, *108*, 4551−4627.

(2) Li, Y.; Chen, X.; Fok, A.; Rodriguez-Cabello, J. C.; Aparicio, C. Biomimetic Mineralization of Recombinamer-Based Hydrogels toward Controlled Morphologies and High Mineral Density. *ACS Appl. Mater. Interfaces* **2015**, *7*, 25784−25792.

(3) Nudelman, F.; Sommerdijk, N. A. J. M. Biomineralization as an Inspiration for Materials Chemistry. *Angew. Chem., Int. Ed.* **2012**, *51*, 6582−6596.

(4) Toffolo, M. B.; Ricci, G.; Caneve, L.; Kaplan-Ashiri, I. Luminescence reveals variations in local structural order of calcium carbonate polymorphs formed by different mechanisms. *Sci. Rep.* **2019**, *9*, No. 16170.

(5) Cuesta Mayorga, I.; Astilleros, J. M.; Fernández-Díaz, L. Precipitation of $CaCO_3$ Polymorphs from Aqueous Solutions: The Role of pH and Sulphate Groups. *Minerals* **2019**, *9*, No. 178.

(6) Neder, M.; Laissue, P. P.; Akiva, A.; Akkaynak, D.; Albéric, M.; Spaeker, O.; Politi, Y.; Pinkas, I.; Mass, T. Mineral formation in the primary polyps of pocilloporoid corals. *Acta Biomater.* **2019**, *96*, 631−645.
(7) Albéric, M.; Bertinetti, L.; Zou, Z.; Fratzl, P.; Habraken, W.; Politi, Y. The Crystallization of Amorphous Calcium Carbonate is Kinetically Governed by Ion Impurities and Water. *Adv. Sci.* **2018**, *5*, No. 1701000.
(8) Ni, M.; Ratner, B. D. Differentiation of Calcium Carbonate Polymorphs by Surface Analysis Techniques - An XPS and TOF-SIMS study. *Surf. Interface Anal.* **2008**, *40*, 1356−1361.
(9) Littlewood, J. L.; Shaw, S.; Peacock, C. L.; Bots, P.; Trivedi, D.; Burke, I. T. Mechanism of Enhanced Strontium Uptake into Calcite via an Amorphous Calcium Carbonate Crystallization Pathway. *Cryst. Growth Des.* **2017**, *17*, 1214−1223.
(10) Long, X.; Ma, Y.; Qi, L. Biogenic and synthetic high magnesium calcite - a review. *J. Struct. Biol.* **2014**, *185*, 1−14.
(11) Checa, A. G. Physical and Biological Determinants of the Fabrication of Molluscan Shell Microstructures. *Front. Mar. Sci.* **2018**, *5*, No. 353.
(12) Spann, N.; Harper, E. M.; Aldridge, D. C. The unusual mineral vaterite in shells of the freshwater bivalve Corbicula fluminea from the UK. *Naturwissenschaften* **2010**, *97*, 743−751.
(13) Wright, S. L.; Thompson, R. C.; Galloway, T. S. The physical impacts of microplastics on marine organisms: a review. *Environ. Pollut.* **2013**, *178*, 483−492.
(14) Deng, Y.; Zhang, Y.; Lemos, B.; Ren, H. Tissue accumulation of microplastics in mice and biomarker responses suggest widespread health risks of exposure. *Sci. Rep.* **2017**, *7*, No. 46687.
(15) Taylor, M. L.; Gwinnett, C.; Robinson, L. F.; Woodall, L. C. Plastic microfibre ingestion by deep-sea organisms. *Sci. Rep.* **2016**, *6*, No. 33997.
(16) Egbeocha, C.; Malek, S.; Emenike, C.; Milow, P. Feasting on microplastics: Ingestion by and effects on marine organisms. *Aquat. Biol.* **2018**, *27*, 93−106.
(17) Ajith, N.; Arumugam, S.; Parthasarathy, S.; Manupoori, S.; Janakiraman, S. Global distribution of microplastics and its impact on marine environment—a review. *Environ. Sci. Pollut. Res.* **2020**, *27*, 25970−25986.
(18) Axworthy, J. B.; Padilla-Gamiño, J. L. Microplastics ingestion and heterotrophy in thermally stressed corals. *Sci. Rep.* **2019**, *9*, No. 18193.
(19) Smith, M.; Love, D. C.; Rochman, C. M.; Neff, R. A. Microplastics in Seafood and the Implications for Human Health. *Curr. Environ. Health Rep.* **2018**, *5*, 375−386.
(20) Bhargava, S.; Chen Lee, S. S.; Min Ying, L. S.; Neo, M. L.; Lay-Ming Teo, S.; Valiyaveettil, S. Fate of Nanoplastics in Marine Larvae: A Case Study Using Barnacles, *Amphibalanus amphitrite*. *ACS Sustainable Chem. Eng.* **2018**, *6*, 6932−6940.
(21) Mahadevan, G.; Valiyaveettil, S. Understanding the interactions of poly(methyl methacrylate) and poly(vinyl chloride) nanoparticles with BHK-21 cell line. *Sci. Rep.* **2021**, *11*, No. 2089.
(22) Du, H.; Amstad, E. Water: How Does It Influence the $CaCO_3$ Formation. *Angew. Chem., Int. Ed.* **2020**, *59*, 1798−1816.
(23) Du, H.; Courrégelongue, C.; Xto, J.; Böhlen, A.; Steinacher, M.; Borca, C. N.; Huthwelker, T.; Amstad, E. Additives: Their Influence on the Humidity- and Pressure-Induced Crystallization of Amorphous $CaCO_3$. *Chem. Mater.* **2020**, *32*, 4282−4291.
(24) Takesue, R. K.; Bacon, C. R.; Thompson, J. K. Influences of organic matter and calcification rate on trace elements in aragonitic estuarine bivalve shells. *Geochim. Cosmochim. Acta* **2008**, *72*, 5431−5445.
(25) Amjad, Z.; Pugh, J.; Reddy, M. M. Kinetic Inhibition of Calcium Carbonate Crystal Growth in the Presence of Natural and Synthetic Organic Inhibitors. *Water Soluble Polymers*; Springer, 2002; pp 131−147.
(26) Sommerdijk, N. A. J. M.; van Leeuwen, E. N. M.; Vos, M. R. J.; Jansen, J. A. Calcium carbonate thin films as biomaterial coatings using DNA as crystallization inhibitor. *CrystEngComm* **2007**, *9*, 1209−1214.
(27) Naka, K.; Chujo, Y. Control of Crystal Nucleation and Growth of Calcium Carbonate by Synthetic Substrates. *Chem. Mater.* **2001**, *13*, 3245−3259.
(28) Bhargava, S.; Chu, J. J. H.; Valiyaveettil, S. Controlled Dye Aggregation in Sodium Dodecylsulfate-Stabilized Poly-(methylmethacrylate) Nanoparticles as Fluorescent Imaging Probes. *ACS Omega* **2018**, *3*, 7663−7672.
(29) Parakhonskiy, B. V.; Yashchenok, A. M.; Donatan, S.; Volodkin, D. V.; Tessarolo, F.; Antolini, R.; Möhwald, H.; Skirtach, A. G. Macromolecule Loading into Spherical, Elliptical, Star-Like and Cubic Calcium Carbonate Carriers. *ChemPhysChem* **2014**, *15*, 2817−2822.
(30) Nakayama, M.; Kajiyama, S.; Kumamoto, A.; Ikuhara, Y.; Kato, T. Bioinspired selective synthesis of liquid-crystalline nanocomposites: formation of calcium carbonate-based composite nanodisks and nanorods. *Nanoscale Adv.* **2020**, *2*, 2326−2332.
(31) Sindhu, S.; Jegadesan, S.; Hairong, L.; Ajikumar, P. K.; Vetrichelvan, M.; Valiyaveettil, S. Synthesis and Patterning of Luminescent $CaCO_3$−Poly(p-phenylene) Hybrid Materials and Thin Films. *Adv. Funct. Mater.* **2007**, *17*, 1698−1704.
(32) Luo, X.; Song, X.; Cao, Y.; Song, L.; Bu, X. Investigation of calcium carbonate synthesized by steamed ammonia liquid waste without use of additives. *RSC Adv.* **2020**, *10*, 7976−7986.
(33) McGann, J.; Willans, M.; Sauzier, G.; Hackett, M. J.; Lewis, S. W.; McGinn, J.; Trubshoe, T.; van Bronswijk, W. Investigating diversity in polymer-based identity cards using ATR-FTIR spectroscopy and chemometrics. *Forensic Sci. Int: Rep.* **2020**, *2*, No. 100149.
(34) Dai, Y.; Zou, H.; Zhu, H.; Zhou, X.; Song, Y.; Shi, Z.; Sheng, Y. Controlled synthesis of calcite/vaterite/aragonite and their applications as red phosphors doped with Eu^{3+} ions. *CrystEngComm* **2017**, *19*, 2758−2767.
(35) Yin, X.; Zhang, J. Flame retardant plasticized poly(vinyl chloride) film with selective solar spectral transparent properties. *RSC Adv.* **2016**, *6*, 46060−46067.
(36) Bruckman, V. J.; Wriessnig, K. Improved soil carbonate determination by FT-IR and X-ray analysis. *Environ. Chem. Lett.* **2013**, *11*, 65−70.
(37) (a) Laipnik, R.; Bissi, V.; Sunc, C. Y.; Falin, G.; Gilbertc, P. U. P. A.; Massa, T. Coral acid rich protein selects vaterite polymorph in vitro. *J. Struct. Biol.* **2020**, *209*, No. 107431. (b) Svenskaya, Y. I.; Fattah, H.; Inozemtseva, O. A.; Ivanova, A. G.; Shtykov, S. N.; Gorin, D. A.; Parakhonskiy, B. V. Key parameters for size-and shape-controlled synthesis of vaterite particles. *Cryst. Growth Des.* **2018**, *18*, 331−337.
(38) Petković, G.; Vukoje, M.; Bota, J.; Preprotić, S. P. Enhancement of Polyvinyl Acetate (PVAc) Adhesion Performance by SiO_2 and TiO_2 Nanoparticles. *Coatings* **2019**, *9*, 707−724.
(39) Shen, Q.; Wei, H.; Wang, L.; Zhou, Y.; Zhao, Y.; Zhang, Z.; Wang, D.; Xu, G.; Xu, D. Crystallization and aggregation behaviors of calcium carbonate in the presence of poly(vinylpyrrolidone) and sodium dodecyl sulfate. *J. Phys. Chem B* **2005**, *109*, 18342−18347.
(40) Wang, H.; Alfredsson, V.; Tropsch, J.; Ettl, R.; Nylander, T. Effect of Polyelectrolyte and Fatty Acid Soap on the Formation of $CaCO_3$ in the Bulk and the Deposit on Hard Surfaces. *ACS Appl. Mater. Interfaces* **2015**, *7*, 21115−21129.
(41) Rodríguez-Navarro, A. B.; Grenier, C.; Checa, A. G.; Jiménez-López, C.; Sánchez-Sánchez, P.; Bertone, D.; Lagos, N. A. Role of the Organic Matter in the Structural Organization of Giant Barnacle Austromegabalanus Psittacus Shell from the Micro- to Nanoscale. *Cryst. Growth Des.* **2021**, *21*, 357−365.
(42) Man, Z.; Muhammad, N.; Sarwono, A.; Bustam, M. A.; Vignesh Kumar, M.; Rafiq, S. Preparation of Cellulose Nanocrystals Using an Ionic Liquid. *J. Polym. Environ.* **2011**, *19*, 726−731.
(43) Rajandas, H.; Parimannan, S.; Sathasivam, K.; Ravichandran, M.; Lee, S. A novel FTIR-ATR spectroscopy based technique for the estimation of low-density polyethylene biodegradation. *Polym. Test.* **2012**, *31*, 1094−1099.

https://doi.org/10.1021/acsomega.1c02564
ACS Omega 2021, 6, 20522−20529

(44) Cao, Z.; Daly, M.; Clémence, L.; Geever, L. M.; Major, I.; Higginbotham, C. L.; Devine, D. M. Chemical surface modification of calcium carbonate particles with stearic acid using different treating methods. *Appl. Surf. Sci.* **2016**, *378*, 320−329.
(45) Eneh, C. I.; Bolen, M. J.; Suarez-Martinez, P. C.; Bachmann, A. L.; Zimudzi, T. J.; Hickner, M. A.; Batys, P.; Sammalkorpi, M.; Lutkenhaus, J. L. Fourier transform infrared spectroscopy investigation of water microenvironments in polyelectrolyte multilayers at varying temperatures. *Soft Matter* **2020**, *16*, 2291−2300.
(46) Yan, G.; Wang, L.; Huang, J. The crystallization behavior of calcium carbonate in ethanol/water solution containing mixed nonionic/anionic surfactants. *Powder Technol.* **2009**, *192*, 58−64.
(47) Finney, A. R.; Innocenti Malini, R.; Freeman, C. L.; Harding, J. H. Amino Acid and Oligopeptide Effects on Calcium Carbonate Solutions. *Cryst. Growth Des.* **2020**, *20*, 3077−3092.
(48) Wei, H.; Shen, Q.; Wang, H.; Gao, Y.; Zhao, Y.; Xu, D.; Wang, D. Influence of segmented copolymers on the crystallization and aggregation of calcium carbonate. *J. Cryst. Growth* **2007**, *303*, 537−545.
(49) Dubey, R. K.; Westerveld, N.; Sudhölter, E. J. R.; Grozema, F. C.; Jager, W. F. Novel derivatives of 1,6,7,12-tetrachloroperylene-3,4,9,10-tetracarboxylic acid: synthesis, electrochemical and optical properties. *Org. Chem. Front.* **2016**, *3*, 1481−1492.
(50) Ihli, J.; Bots, P.; Kulak, A.; Benning, L. G.; Meldrum, F. C. Elucidating Mechanisms of Diffusion-Based Calcium Carbonate Synthesis Leads to Controlled Mesocrystal Formation. *Adv. Funct. Mater.* **2013**, *23*, 1965−1973.

https://doi.org/10.1021/acsomega.1c02564
ACS Omega 2021, 6, 20522−20529